Real-time attack on single *Escherichia coli* cells by the human antimicrobial peptide LL-37

Kem A. Sochacki[a], Kenneth J. Barns[a], Robert Bucki[b], and James C. Weisshaar[a,1]

[a]Department of Chemistry, University of Wisconsin, Madison, WI 53706; and [b]Department of Physiology and the Institute for Medicine and Engineering, University of Pennsylvania, Philadelphia, PA 19104

Edited by Jennifer Lippincott-Schwartz, National Institutes of Health, Bethesda, MD, and approved March 10, 2011 (received for review January 21, 2011)

Natural antimicrobial peptides (AMPs) provide prototypes for the design of unconventional antimicrobial agents. Existing bulk assays measure AMP activity but do not provide details of the growth-halting mechanism. We use fluorescence microscopy to directly observe the attack of the human antimicrobial peptide LL-37 on single *Escherichia coli* cells in real time. Our findings strongly suggest that disruption of the cytoplasmic membrane is not the growth-halting mechanism. At 8 μM, LL-37 binding saturates the outer membrane (OM) within 1 min. Translocation across the OM and access to the periplasmic space (5–25 min later) correlates in time with the halting of growth. Septating cells are attacked more readily than nonseptating cells. The halting of growth may occur because of LL-37 interference with cell wall biogenesis. Only well after growth halts does the peptide permeabilize the cytoplasmic membrane to GFP and the small dye Sytox Green. The assay enables dissection of antimicrobial design criteria into two parts: translocation across the OM and the subsequent halting of growth.

In US hospitals in 2002, microbial infections were acquired by some 4.5% of admitted patients (1.7 million infections annually) (1). In aggregate, such infections are now the sixth leading cause of death in the United States. Infections by multidrug-resistant Gram-negative bacteria such as *Pseudomonas aeruginosa*, *Acinetobacter baumannii*, and a host of *Enterobacteriaceae* are particularly troublesome. These pathogens are notorious for their low susceptibility to many drugs through a variety of inherent cellular as well as genetically transferable mechanisms. Greater antibiotic resistance in Gram-negative species may arise from the presence of an outer membrane (OM) decorated with lipopolysaccharides (LPSs) and an O-antigen layer in addition to the cytoplasmic membrane (CM).

In the search for innovative antimicrobial strategies, nature provides intriguing prototypes in the form of the antimicrobial peptides (AMPs). More than 1,200 bacteria-targeting AMPs have been discovered in a diverse set of organisms from mammals and amphibians to insects and microbes themselves (2). Cationic, amphipathic AMPs provide appealing models in that they target and permeabilize the negatively charged membranes of both Gram-negative and -positive bacteria while inflicting much less damage on the zwitterionic membranes of eukaryotic cells (3). Such a general biophysical attack on the bacterial cell envelope is relatively insusceptible to resistance by mutation. Conventional wisdom holds that AMPs halt bacterial growth by disrupting the barrier function of the cytoplasmic membrane. However, this view has been questioned recently (4). Many laboratories are working to develop synthetic analogs of AMPs as antimicrobial agents (5, 6). The assay described here will enable direct comparison of the mechanisms of natural AMPs with those of synthetic analogs on the single-cell level.

The human cathelicidin LL-37, discovered 15 y ago (7), has the 37-residue sequence LLGDFFRKSKEKIGKEFKRIVQRIKDFLRNLVPRTES. At neutral pH, the peptide is highly charged, with 11 positive and 5 negative residues (net charge of +6). Although unstructured in pure water, it exhibits α-helical secondary structure in physiologically relevant solutions or when bound to lipid bilayer surfaces. The resulting helix is amphipathic, which encourages oligomerization in solution (8). LL-37 is an integral part of the human innate immune system, playing roles that go beyond its antimicrobial properties (9). It is expressed in many different types of cells, including leukocytes, bone marrow, and lung and colon epithelia. It is also found in sweat, saliva, and breast milk among other body fluids (8). Decreased activity of LL-37 is implicated in the chronic bacterial infections common in patients with cystic fibrosis (10).

Our current understanding of how this AMP attacks bacteria has been shaped by bulk assays (11, 12), model membrane assays (13–18), and assumptions based on studies of other AMPs. Minimum inhibitory concentration (MIC) assays, which determine the lowest concentration of peptide that inhibits bacterial growth, show that LL-37 is effective against a broad spectrum of bacteria that is both Gram-positive and -negative (12). In vitro assays using lipid bilayers indicate that LL-37 permeabilizes model membranes by a carpeting or toroidal pore mechanism (13–17).

The detailed antimicrobial mechanism of LL-37 remains unclear. Here, we use time-resolved fluorescence microscopy to dissect the course of events as LL-37 attacks single cells of the Gram-negative species *Escherichia coli* (K-12) and halts growth. In effect, the method provides a single-cell, time-resolved MIC assay that enables us to correlate, in real time, the degree of LL-37 binding, its spatial distribution, the permeabilization of the OM and CM, and the halting of cell growth. Direct measurements of this type are poised to provide an enhanced understanding of how AMPs attack bacterial cells as well as guide design criteria for synthetic agents.

Results and Discussion

In two-color experiments using time-lapse imaging over 1 h, LL-37 is labeled with a red-fluorescing Rhodamine dye (Rh-LL-37), enabling us to monitor total LL-37 binding and its spatial distribution vs. time. The green channel monitors emission from two species: GFP, which has been exported to the periplasm (the ~40-nm-thick space between the OM and CM) by the twin arginine translocase pathway (19, 20), and the DNA stain Sytox Green. When the OM becomes permeabilized to GFP, the thin periplasmic GFP image disappears. When the CM becomes permeabilized to Sytox Green, the dye enters the cytoplasm, binds to DNA, and fluoresces strongly. Interleaved observations by phase contrast microscopy enable measurement of tip to tip cell length vs. time, a direct readout of cell growth (*Methods*). Thus far, we have focused primarily on LL-37 at 8 μM, four times higher than the long-term bulk MIC, to observe growth-halting symptoms on a convenient imaging timescale.

Author contributions: K.A.S. and J.C.W. designed research; K.A.S. and K.J.B. performed research; R.B. contributed new reagents/analytic tools; K.A.S. analyzed data; and K.A.S. and J.C.W. wrote the paper.

The authors declare no conflict of interest.

[1]To whom correspondence should be addressed. E-mail: weisshaar@chem.wisc.edu.

See Author Summary on page 6347.

This article contains supporting information online at www.pnas.org/lookup/suppl/doi:10.1073/pnas.1101130108/-/DCSupplemental.

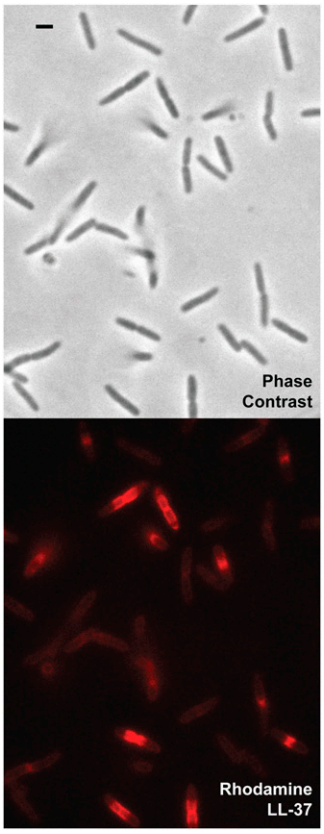

Fig. 1. Preferential phase 2 attack on septating cells at t = 12 min after exposure to 8 μM Rh-LL-37. The phase contrast image (*Upper*) shows cells at different phases of the cell cycle; septating cells look pinched at the midplane. The red fluorescence image (*Lower*) shows bright bands of Rh-LL-37 centered on the midplane of septating cells (phase 2 attack). Nonseptating cells exhibit only a dim, uniform coating of Rh-LL-37 (phase 1 attack). (Scale bar, 2 μm.)

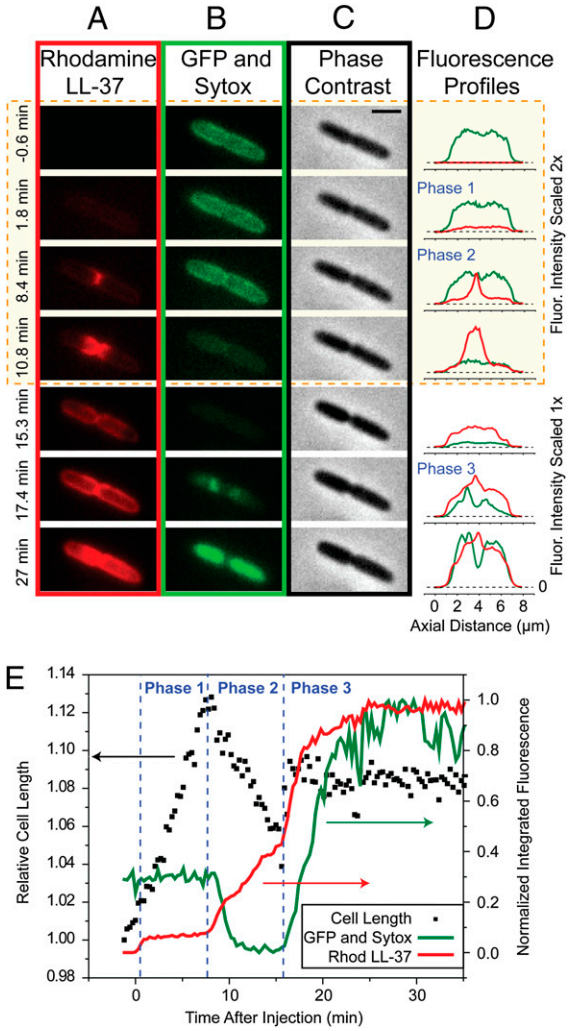

Fig. 2. Sequence of events during attack by Rh-LL-37 at 8 μM of a single septating *E. coli* cell expressing periplasmic GFP. Medium also contains Sytox Green at 5 nM. The snapshots are taken from a single movie at the times shown at left. (Scale bar, 2 μm.) (*A*) Red fluorescence channel (Rh-LL-37), (*B*) green fluorescence channel (periplasmic GFP and then Sytox Green on entry to cytoplasm), and (*C*) phase contrast images (monitoring cell growth). The first four time points are shown with two times intensity in both red and green for clarity. (*D*) Axial intensity profiles of red and green channels. (*E*) Total intensity of green and red fluorescence associated with the cell (right scale) and relative length of the cell from phase contrast images (left scale) vs. time over 35 min. Phases 1–3 of the attack are labeled. Fluorescence intensities are background corrected.

A snapshot of a field of cells exposed to 8 μM of Rh-LL-37 for 12 min is shown in Fig. 1. Importantly, cells that are visibly septating at t = 0 (those preparing to divide) stop growing much sooner than nonseptating cells. The heterogeneity in degree of binding and spatial distribution of Rh-LL-37 is striking. Septating cells are brighter than nonseptating cells and exhibit an intense region of Rh-LL-37 fluorescence in a banded pattern centered at the septum. Almost all cells that are visibly septating at t = 0 have stopped growing at t = 12 min, whereas growth continues for most nonseptating cells.

For each cell, Rh-LL-37 exhibits three distinct phases of binding corresponding to increasing depth of penetration of the Gram-negative cell envelope; 1 h of time-lapse imaging of a typical septating cell in the presence of 8 μM Rh-LL-37 and 5 nM Sytox Green is shown in Movie S1. The snapshots and axial intensity plots of Fig. 2 *A*–*D* show the spatial distribution of LL-37, GFP, and Sytox Green as well as the phase contrast images during the three phases of attack. The green intensity plots show the abrupt loss of periplasmic GFP at t = 9 min and the abrupt permeabilization of the CM to Sytox Green at t = 16 min. The correlation in time of these events with the halting of growth is shown in Fig. 2*E*. The heterogeneity of behavior observed for several different cells in a single experiment can be seen in Movie S2.

LL-37 must attack the cell from the outside in; we infer that phase 1 involves binding of the positively charged LL-37 to the negatively charged LPS layer on the outside of the OM. Accordingly, for both septating and nonseptating cells, phase 1 binding begins immediately after exposure to Rh-LL-37 and coats the cell periphery uniformly. Some 70% of the fluorescence intensity of phase 1 can be rinsed away with fresh media lacking Rh-LL-37 (Fig. S1).

In septating cells, phase 2 binding exhibits surprising spatial and temporal evolution (Fig. 2 *A*, *D*, and *E*). The early spatial distribution of phase 2 is a narrow circumferential band at the nascent septum that slowly spreads axially out across the entire cell length over 5–10 min while maintaining a halo-like distribution (that of a thin shell). Importantly, growth halts at the beginning or shortly after the onset of this phase. Because phase 1 binds to the outside of the cell and phase 3 abruptly permeabilizes the CM to LL-37, GFP, and Sytox Green (see below), we infer that phase 2 involves LL-37 crossing the OM to gain access to new binding sites within the thin periplasmic space. The exit of GFP from the periplasm after both the onset of phase 2 and the halting of growth indicates that LL-37 translocates across the OM before formation of GFP-sized pores. It remains possible that

LL-37 translocates across the OM by formation of smaller pores, either permanent or transient, which would be expected in a toroidal pore model of AMP attack (21).

Evidently, LL-37 translocation across the OM is much more facile at the nascent curved membrane of the septum than at the more mature cylindrical or end-cap regions. If LL-37 diffused freely within the periplasm after translocation, the thin space would fill in a few seconds (20). Instead, we attribute the slow expansion of phase 2 to continual entry into the periplasmic space at the septal region followed by prompt binding to immobile elements there. As local binding sites saturate, entering molecules must search farther and farther out to find additional binding sites. A plausible binding partner is the peptidoglycan layer, which is the cell shape-determining meshwork of sugars and peptides between the OM and CM. In separate tests in vitro, we have shown that Rh-LL-37 indeed binds to peptidoglycan (*Methods*).

The onset of phase 3 clearly involves penetration of the CM by LL-37 and prompt permeabilization to the small dye molecule Sytox Green (Fig. 2 *B*, *D*, and *E*). Sytox commonly enters the cytoplasm near the septum and binds first to the nearby DNA, indicating that the septal region of the CM is also especially permeable to LL-37. Composite information from separate experiments (Fig. S2) shows that cytoplasmic GFP (27 kDa), Rh-LL-37 (4.9 kDa), and Sytox Green (1 kDa) all cross the CM at the same time, namely, at the onset of phase 3 binding.

Thus, the data suggest that the initial growth-halting mechanism is not permeabilization of the CM. For septating cells, the halting of growth occurs early in phase 2, which is judged by phase contrast measurements of cell length vs. time (Fig. 2*E*). For 8 μM Rh-LL-37, this often occurs minutes before periplasmic GFP is lost and always occurs at least 3 min before the CM is permeabilized to GFP, Rh-LL-37, and Sytox Green. The underlying cause of the halting of growth remains uncertain, and indeed, it may differ from cell to cell. A specific biochemical mechanism such as the targeting of particular enzymes seems unlikely, because the *D* and *L* stereoisomers of several cationic α-helical AMPs have shown very similar antibacterial activity (22). Indeed, we have found that the *D* and *L* stereoisomer of unlabeled LL-37 (both with an amidated C terminus) and the *L* stereoisomer lacking a C-terminal amide all behave similarly in our single-cell fluorescence assay and exhibit the same MIC in our conditions. One plausible biophysical growth-halting mechanism is interference with the synthesis of the new curved cell envelope (the OM, CM, peptidoglycan layer, and LPS layer) at the septal region. Binding of LL-37 to the negatively charged peptide cross-links between glycan strands could interfere with enzymatic action. The fact that LL-37 indeed binds to purified peptidoglycan in vitro supports this mechanism (*Methods*).

Cells that are not septating at $t = 0$ also exhibit three phases of LL-37 binding, but phases 2 and 3 occur later after injection. This is illustrated in Fig. 3, which summarizes the timeline of events for 20 cells within a single experiment. The onset of phases 2 and 3 was determined from plots of total Rh-LL-37 intensity vs. time, as in Fig. 2*E*. The time of periplasmic GFP loss was measured as the frame in which the green intensity associated with the cell dropped to one-half of its original value. The halting of growth was determined from the abrupt change in slope of plots of cell length vs. time (Fig. 2*E*). When the cells are organized in order of the time of the onset of phase 2 and categorized based on the timing of visible septation, a trend emerges. Later onset of phase 2 correlates with cells that exhibit septation later in the experiment (or not at all). All cells that show evidence of septation at any time during the 60-min observation period exhibit septal localization of Rh-LL-37 at the beginning of phase 2 binding. For these cells, it seems likely that initiation of cell division enables phase 2 of the Rh-LL-37 attack. When the septal attack of Rh-LL-37 occurs later, there is often a longer lag between the beginning of phase 2 and the halting of growth. For the small subset of cells that never exhibits visible septation, phase 2 is spatially more diffuse and not always centered along the cell axis (Fig. S3). Even these cells may be attacked at an early stage of division before clear evidence of a septum is observable.

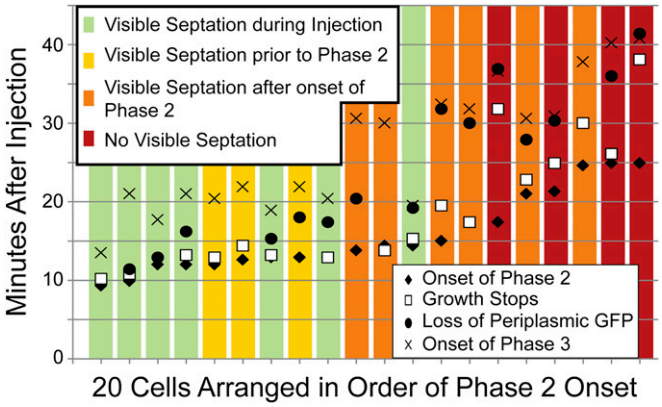

Fig. 3. The timeline of events for 20 cells in a single experiment. Cells contained periplasmic GFP and were attacked by 8 μM Rh-LL-37. There was no Sytox Green present. The cells were split into four categories based on when septation was visible by eye in the phase contrast channel. Septation likely begins before the time at which it is observable. Phase 2 begins later for cells that are not septating at the beginning of the experiment. In most cases, phase 2 seems to be enabled by the onset of septation. In a few cases for which visible septation is never observed, phase 2 still occurs but is more diffuse in space (Fig. S3). In cases where an event is not shown for a given cell, that event was not analyzable.

We tested for effects of the Rhodamine label on LL-37 activity. Both LL-37 and Rh-LL-37 exhibit a bulk MIC of 2 μM after 12 h (Fig. S4). In the fluorescence microscopy experiments, the same symptoms (translocation of LL-37 across the OM, permeabilization of the OM to periplasmic GFP, and entry of Sytox Green into the cytoplasm) are observed with and without the label. However, unlabeled LL-37 evidently translocates across the OM more rapidly than Rh-LL-37. In the experiments with unlabeled LL-37 and periplasmic GFP and Sytox Green present, the GFP sometimes moves in to fill the cytoplasm before leaving the cell entirely. When this occurs, entry of Sytox into the cytoplasm and complete loss of GFP from the cell occur essentially simultaneously and only after periplasmic GFP has gained access to the cytoplasm. This sequence of events indicates that LL-37 can translocate across the OM without opening pores large enough to permit passage of either periplasmic GFP or external Sytox Green. As a final test, we flowed Rhodamine B at 8 μM over cells in the absence of LL-37. Cell growth continued for the entire 1 h of observation, GFP remained in the periplasm, and Sytox Green never entered the cytoplasm. The Rhodamine B was easily rinsed away at the end of the experiment with no evidence of binding. Evidently, Rhodamine B itself has no effect on K-12 *E. coli*. Additionally, we performed a control without Sytox Green, which ensured that the DNA stain did not change the sequence of events that we have described (Fig. S5).

In preliminary experiments at 2 μM Rh-LL-37, comparable with the 12-h MIC, phase 1 binding slowly increased over ~4 min (as opposed to <1 min at 8 μM). phase 2 binding was observed in <1% of the cells on a 1-h timescale. This suggests that translocation across the OM requires a critical threshold concentration of LL-37 bound to the OM surface.

Finally, the K-12 strain of *E. coli* studied here lacks the O-antigen layer common to most pathogenic strains. To test its importance, we carried out analogous experiments on an HS strain of *E. coli* (23), which does have an O-antigen layer. The three-phase attack of Rh-LL-37 was again observed on a similar timescale in essentially the same fashion.

The present assay in which the AMP is constantly present provides a single-cell time-resolved analog of the MIC assay. Although we have dissected the attack into multiple phases, an important remaining question is which phase of the attack is lethal. At which point in time would removal of external LL-37 and restoration of aerated growth medium enable individual cells to recover and grow? Perhaps phase 2 of the attack is recoverable, whereas phase 3 is not. The bulk assay for the minimum bactericidal concentration (MBC) determines the concentration at which exposure to the AMP causes loss of viability, even after returning the cells to aerated growth medium lacking the AMP (24). A single-cell time-resolved recovery assay analogous to the MBC assay is under development.

In summary, we have shown that relatively straightforward fluorescence methods can provide incisive mechanistic information on the degradation of membrane function by natural AMPs. For the example of LL-37 attacking the Gram-negative bacteria *E. coli*, the antimicrobial activity can be dissected into stages. The first stage is binding to the OM and its LPS and O-antigen layers, which quickly saturate. The halting of growth occurs shortly after entry of LL-37 into the periplasmic space. Nascent septal membranes are particularly susceptible to LL-37 penetration. The assay should prove useful in the design of synthetic antimicrobial agents based first on their ability to penetrate the OM and second on their ability to halt growth after access to the periplasm or cytoplasm is achieved. These methods are immediately applicable to studies of Gram-positive bacteria and pathogenic species. The plethora of natural AMPs may well use a variety of growth-halting mechanisms that differ substantially from that of LL-37.

Methods

Materials, Strains, and Growth Conditions. Rhodamine LL-37 (no C-terminal amide) and unlabeled LL-37 (C-terminal amidated) were both purchased from Bachem (4049885 and H-6224, respectively). Unlabeled LL-37 lacking a C-terminal amide was purchased from Anaspec (61302). The *D* enantiomer of LL-37 (with a C-terminal amide) was made by the University of Wisconsin Biotechnology Center. All peptides were purchased at >85% purity and used without further purification.

The *E. coli* strain is K12, MG1655. For experiments on periplasmic GFP, TorA-GFP was expressed from the plasmid pJW1 as previously described (20). TorA-GFP consists of a short sequence (43 residues) from trimethylamine *N*-oxide (TMAO) reductase that signals the twin-arginine translocase pathway. The signal sequence is cleaved from GFP on transport to the periplasm (19). For experiments on cytoplasmic GFP, we used the plasmid pMGS053, which expresses GFPmut2 using the *lac* promoter with repression maintained by pREP4 (Qiagen), as previously described (25). The WT MG1655 strain (lacking the plasmid) was used for several control experiments. In addition, the *E. coli* HS strain (23), which has an O-antigen layer, was obtained from Rodney Welch (University of Wisconsin, Madison, WI). All cultures were grown in EZ rich defined medium (EZRDM), which consists of a MOPS-buffered solution (M2130; Teknova), glucose (2 mg/mL), supplemental amino acids and vitamins (M2104; Teknova), nucleic acids (M2103; Teknova), 1.32 mM K_2HPO_4, and 76 mM NaCl (26). Cultures were grown from glycerol frozen stock to stationary phase overnight. Subcultures were grown to exponential phase and plated on glass for imaging.

Flow Chamber. The flow chamber is made of a lower 22- × 40-mm coverslip and an upper 22- × 22-mm coverslip that sandwich a silicon gasket (two 325-μm blank gaskets from Warner Instruments stacked together). The gasket has a 3- × 31-mm slot that makes up the ∼60 μL volume of the flow chamber. A plastic piece above the top coverslip contains ports to allow fluid to enter and exit the chamber on either side. The entire assembly is pressed together by an aluminum base and top pressure plate. The chamber is maintained at 30 °C with a TC-344B dual automatic temperature controller through the CC-28 cable assembly attached to RH-2 heater blocks (Warner Instruments).

The coverslips are cleaned with 30 min of sonication in acetone and 30 min of sonication in 1 M KOH. They are then soaked in 0.01% poly-L-lysine (molecular weight > 150,000) for 20 min to aid cell adhesion. Thorough rinsing with filtered deionized water occurs after each step. Cells were injected into the prewarmed chamber straight from a growing culture. They were allowed to adhere to the poly-L-lysine–coated coverslip to a target cell density of roughly 1 cell/60 μm^2, after which the remaining cells were rinsed away with fresh growth medium. In the absence of antimicrobial peptide, the *E. coli* length doubles in ∼85 min on the coverslip over the observation period of 1.5 h. In comparison, the doubling time in bulk is ∼50 min and is measured by OD.

Microscopy. All microscopy was performed on a Nikon TE300 inverted microscope with a 100× 1.3 NA phase contrast objective (Nikon). Postmicroscope images were further magnified 1.45× in a home-built magnification box. A 488-nm Ar^+ laser (Melles Griot) was expanded to broadly illuminate a 56-μm diameter circular region of sample for excitation of both GFP and Sytox Green (Invitrogen). A 561-nm laser (CrystaLaser) was likewise expanded for excitation of Rhodamine LL-37. A 1-h-long movie with 600 frames of 50 ms exposure, each 6 s apart, was obtained with an Andor iXon 897 EMCCD camera. The pixel size corresponds to 110 ± 10 nm at the sample. The imaging sequence cycled among 488 nm fluorescence excitation, 561 nm fluorescence excitation, and phase contrast illumination with each sequence repeated every 18 s. All emission filters were purchased from Chroma Technology. A 500-nm long-pass emission filter (HQ500LP) was always present. Bandpass emission filters (HQ510/20M for the 488-nm laser green channel, HQ600/50M for the 561-nm laser red channel, and no bandpass filter for phase contrast) were cycled with a FW102 filter wheel from Thorlabs. The movie began after adhesion of cells and the rinsing away of extra cells. The cells were imaged for ∼1.5 min before injection of fresh medium (EZRDM) containing LL-37 or Rhodamine LL-37, with Sytox Green (5 nM) included when desired. This solution was made immediately before the experiment and was vortexed (3,200 rpm, Vortex Genie 2; Scientific Industries) for at least 10 s to avoid large LL-37 aggregates. Injection took place over ∼20 s. The remainder of the movie imaged the effects of LL-37 on the cells.

Fluorescence Profiles and Measurement of Cell Length. All images were acquired with Andor Solis software and further analyzed in ImageJ (27) and MATLAB (Mathworks). The spatial coordinate along the long axis of the cell is called *z*. Axial fluorescence intensity profiles were obtained from a rectangle that surrounded the entire cell (long axis parallel to the *z* axis of the cell). The intensities of the pixels transverse to the *z* axis were averaged to yield the axial profile vs. *z*. An analogous profile of the phase contrast image was created to measure changes in the length of the cell as a function of time. Before creating a profile, each frame of the movie was rotated separately with bilinear interpolation to obtain the same cell orientation throughout the entire movie. Using MATLAB, a cubic spline was fit to the phase contrast axial profile. In each frame, cell length was determined as the full width at half-maximum height of the phase contrast axial profile. We estimate that changes in cell length can, thus, be measured to an accuracy of about ± 50 nm.

MIC Assay. MICs were determined using a broth microdilution method. A serial dilution of LL-37 or Rh-LL37 was performed in separate rows of a polystyrene 96-well plate in 1× EZRDM containing an inoculum of *E. coli* MG1655 or HS (100 μL total). The inoculum was a 1:20 dilution from broth culture at midlog phase (OD_{600} = 0.5) grown at 30 °C. To serve as controls, each assay included a similar serial dilution of ampicillin (8 wells with cells and no antimicrobial and 5 wells with medium but no cells and no antimicrobial agent). The plate was incubated at 30 °C and shaken at 200 rpm in a Lab-Line Orbital Environ Shaker (Model 3527) for up to 24 h. The MIC is reported as the lowest concentration for which no cell growth could be detected as determined by measurements of OD at 595 nm using a Wallac EnVision 2100 Multilabel Reader from Perkin-Elmer.

Peptidoglycan Binding Assay. The binding of Rhodamine LL-37 to purified peptidoglycan from *E. coli* K12 (InvivoGen) was observed qualitatively by fluorescence microscopy. Three solutions were prepared: (*i*) 8 μM Rhodamine LL-37 with ∼0.5 mg/mL peptidoglycan in EZRDM, (*ii*) ∼0.5 mg/mL peptidoglycan in EZRDM (no Rh-LL-37), and (*iii*) 8 μM Rhodamine LL-37 (no peptidoglycan) in EZRDM. Each solution was spun down at 5,585 × *g* for 10 min. After removal of the supernatant, the remainder was resuspended into fresh EZRDM. When peptidoglycan was present, there was a visible pellet. Each resuspension was placed on a glass slide, covered with a coverslip, and sealed with nail polish. Visible aggregates of peptidoglycan were visible in the microscope in phase contrast when peptidoglycan was present in the original mixture. In the resuspensions of solution *i*, the peptidoglycan aggregates exhibited 16–53 times more fluorescence in the red channel than the resuspensions of solution *ii*. The resuspensions of solution *iii* exhibited very low fluorescence.

ACKNOWLEDGMENTS. We thank Dr. Rodney Welch from the University of Wisconsin—Madison for the HS strain. This work was generously supported by National Institute of General Medical Sciences Grants R01GM086468 (from the American Recovery and Reinvestment Act) and R01GM094510.

1. Peleg AY, Hooper DC (2010) Hospital-acquired infections due to gram-negative bacteria. *N Engl J Med* 362:1804–1813.
2. Wang G (2011) The Antimicrobial Peptide Database. Available at http://aps.unmc.edu/AP/main.php. Accessed September 23, 2010.
3. Tossi A, Sandri L, Giangaspero A (2000) Amphipathic, α-helical antimicrobial peptides. *Biopolymers* 55:4–30.
4. Brogden KA (2005) Antimicrobial peptides: Pore formers or metabolic inhibitors in bacteria? *Nat Rev Microbiol* 3:238–250.
5. Mowery BP, et al. (2007) Mimicry of antimicrobial host-defense peptides by random copolymers. *J Am Chem Soc* 129:15474–15476.
6. Wang G, Li X, Wang Z (2009) APD2: The updated antimicrobial peptide database and its application in peptide design. *Nucleic Acids Res* 37:D933–D937.
7. Gudmundsson GH, et al. (1996) The human gene FALL39 and processing of the cathelin precursor to the antibacterial peptide LL-37 in granulocytes. *Eur J Biochem* 238:325–332.
8. Dürr UH, Sudheendra US, Ramamoorthy A (2006) LL-37, the only human member of the cathelicidin family of antimicrobial peptides. *Biochim Biophys Acta* 1758: 1408–1425.
9. Bucki R, Leszczyńska K, Namiot A, Sokołowski W (2010) Cathelicidin LL-37: A multitask antimicrobial peptide. *Arch Immunol Ther Exp (Warsz)* 58:15–25.
10. Bucki R, Byfield FJ, Janmey PA (2007) Release of the antimicrobial peptide LL-37 from DNA/F-actin bundles in cystic fibrosis sputum. *Eur Respir J* 29:624–632.
11. Johansson J, Gudmundsson GH, Rottenberg ME, Berndt KD, Agerberth B (1998) Conformation-dependent antibacterial activity of the naturally occurring human peptide LL-37. *J Biol Chem* 273:3718–3724.
12. Turner J, Cho Y, Dinh NN, Waring AJ, Lehrer RI (1998) Activities of LL-37, a cathelin-associated antimicrobial peptide of human neutrophils. *Antimicrob Agents Chemother* 42:2206–2214.
13. Oren Z, Lerman JC, Gudmundsson GH, Agerberth B, Shai Y (1999) Structure and organization of the human antimicrobial peptide LL-37 in phospholipid membranes: Relevance to the molecular basis for its non-cell-selective activity. *Biochem J* 341:501–513.
14. Porcelli F, et al. (2008) NMR structure of the cathelicidin-derived human antimicrobial peptide LL-37 in dodecylphosphocholine micelles. *Biochemistry* 47:5565–5572.
15. Neville F, et al. (2006) Lipid headgroup discrimination by antimicrobial peptide LL-37: Insight into mechanism of action. *Biophys J* 90:1275–1287.
16. Gable JE, Schlamadinger DE, Cogen AL, Gallo RL, Kim JE (2009) Fluorescence and UV resonance Raman study of peptide-vesicle interactions of human cathelicidin LL-37 and its F6W and F17W mutants. *Biochemistry* 48:11264–11272.
17. Morgera F, et al. (2009) Primate cathelicidin orthologues display different structures and membrane interactions. *Biochem J* 417:727–735.
18. Epand RF, Wang G, Berno B, Epand RM (2009) Lipid segregation explains selective toxicity of a series of fragments derived from the human cathelicidin LL-37. *Antimicrob Agents Chemother* 53:3705–3714.
19. Thomas JD, Daniel RA, Errington J, Robinson C (2001) Export of active green fluorescent protein to the periplasm by the twin-arginine translocase (Tat) pathway in Escherichia coli. *Mol Microbiol* 39:47–53.
20. Sochacki KA, Shkel IA, Record MT, Weisshaar JC (2011) Protein diffusion in the periplasm of *E. coli* under osmotic stress. *Biophys J* 100:22–31.
21. Ludtke SJ, et al. (1996) Membrane pores induced by magainin. *Biochemistry* 35: 13723–13728.
22. Maloy WL, Kari UP (1995) Structure-activity studies on magainins and other host defense peptides. *Biopolymers* 37:105–122.
23. Levine MM, et al. (1978) *Escherichia coli* strains that cause diarrhea but do not produce heat-labile or heat-stable enterotoxins and are non-invasive. *Lancet* 1:1119–1122.
24. Andrews JM (2001) Determination of minimum inhibitory concentrations. *J Antimicrob Chemother* 48(Suppl 1):5–16.
25. Konopka MC, et al. (2009) Cytoplasmic protein mobility in osmotically stressed Escherichia coli. *J Bacteriol* 191:231–237.
26. Neidhardt FC, Bloch PL, Smith DF (1974) Culture medium for enterobacteria. *J Bacteriol* 119:736–747.
27. Rasband WS (2011) Image J. Available at http://rsb.info.nih.gov/ij/. Version 1.44.